ChemComm

ROYAL SOCIETY OF CHEMISTRY

COMMUNICATION

View Article Online
View Journal | View Issue

Cite this: *Chem. Commun.*, 2026, **62**, 4358

Received 31st October 2025,
Accepted 2nd February 2026

DOI: 10.1039/d5cc06213f

rsc.li/chemcomm

Ultrafast photothermal shock for crystallization of vanadium oxide and *in situ* anchoring of Co single atoms for enhanced oxygen evolution reaction

Dogyeong Jeon,[a] Heejun Park,[a] Jong Won Baek,[a] Ki Ro Yoon,[b] Sang-Joon Kim*[c] and Il-Doo Kim *[a]

An ultrafast photothermal shock simultaneously crystallizes amorphous vanadium oxide and anchors Co single-atoms, kinetically suppressing atomic aggregation within milliseconds. Featuring a vanadium oxide crystalline phase tunable by the applied shock energy and a photothermal temperature reaching 1600 °C, the resulting self-supported electrode demonstrates a proof-of-concept application as a catalyst for the electrochemical oxygen evolution reaction, establishing an efficient route toward advanced single-atom catalysts.

Single-atom catalysts (SACs) represent a paradigm shift in heterogeneous catalysis, offering the ultimate atom-utilization efficiency and unique electronic properties derived from their low-coordination environment, which can lead to exceptional catalytic activity and selectivity exceeding their nanoparticle counterparts.[1,2] The performance of SACs is intrinsically linked to the support material, which not only anchors the metal atoms to prevent aggregation but also provides electrochemical robustness and facilitates efficient charge transfer.[3,4] Beyond structural stabilization, the support often plays an active electronic role by modulating the oxidation state and coordination environment of the anchored atoms through metal–support interactions, defect formation, and charge redistribution at the interface.[5] Although carbon supports facilitate interfacial charge transfer, their practical application in the oxygen evolution reaction (OER) is severely restricted by their vulnerability to corrosion under high anodic potentials.[6–8] This limitation has spurred the exploration of more robust transition metal compounds as attractive alternatives capable of optimizing reaction kinetics and ensuring long-term electrochemical stability.[9–11]

Among the vast family, vanadium oxides stand out as an exceptionally promising class of materials for catalytic applications, existing with different stoichiometries (*e.g.*, V_2O_5, VO_2, V_6O_{13}, V_2O_3) due to the multiple accessible oxidation states of vanadium (from +2 to +5).[12] Furthermore, the crystalline phase provides significantly enhanced structural stability and higher intrinsic electronic conductivity compared to its amorphous counterpart, which is essential for ensuring long-term durability and efficient charge transport in an electrocatalytic system.[13–15] For instance, a recent study has demonstrated that highly crystalline $V_2O_5{\cdot}nH_2O$ serve as exceptionally effective hosts for Co SACs, showing significant potential for the OER.[16] This high performance is attributed to the synergistic interaction between the Co sites and the crystalline vanadium oxide support, facilitated by the support's superior structural robustness and well-defined interlayer channels. However, despite this compelling potential, the synthesis of SACs on crystalline vanadium oxide faces a persistent thermodynamic challenge and requires a time-consuming process. The transformation from amorphous vanadium oxide precursors to highly ordered crystalline phases necessitates overcoming substantial activation energy barriers for nucleation and crystal growth, while simultaneously preventing the undesirable, thermodynamically favored aggregation of metal atoms. Conventional equilibrium-driven synthesis routes such as furnace annealing require long-duration thermal treatments (several hours) to achieve high crystallinity.[17] Furthermore, this extended high-temperature exposure promotes undesirable cluster formation, thereby limiting the maximum metal loading achievable in SACs.[18–20] Consequently, this reliance on time-intensive, equilibrium-based processes highlights a major bottleneck in terms of synthesis efficiency and scalability, leading to a clear need for fundamentally different, non-equilibrium strategies that can simultaneously yield a highly crystalline support and stabilize atomically dispersed catalysts against aggregation.

Our previous work has established ultrafast photothermal shock as a versatile, kinetically controlled non-equilibrium-driven synthesis platform, demonstrating its utility in synthesizing

[a] *Department of Materials Science and Engineering, Korea Advanced Institute of Science and Technology (KAIST), 291 Daehak-ro, Yuseong-gu, Daejeon 34141, Republic of Korea. E-mail: jepro1012@kaist.ac.kr, idkim@kaist.ac.kr*
[b] *Department of Materials Science and Engineering, Konkuk University, 120, Neungdong-ro, Gwangjin-gu, Seoul 05029, Republic of Korea*
[c] *Department of Materials Science and Engineering, Chungnam National University (CNU), 99 Daehak-ro, Yuseong-gu, Daejeon 34134, Republic of Korea. E-mail: sangjoon@cnu.ac.kr*

high-entropy alloy on carbon nanofibers (CNFs) as well as anchoring a wide variety of single atoms (*e.g.*, Co, Ni, Pt) onto N-doped graphene supports under ambient conditions, bypassing the need for vacuum systems.[21,22] More recently, we further extended this strategy to enable the simultaneous, millisecond-scale transformation of nanodiamonds into carbon nanoonions and the concurrent anchoring of SACs onto these newly formed nanostructures.[23] Building upon this foundation, herein we apply an ultrafast photothermal shock strategy (1600 °C within 20 ms), utilizing an intense pulse of light from a Xenon lamp, to fabricate Co SACs anchored on a highly crystalline, electrodeposited vanadium oxide/carbon nanofiber electrode (Co/VO_x/CNF). The black CNF scaffold absorbs the incident light and converts it into localized heat, thereby photothermally crystallizing the VO_x layer conformally coated on the CNF surface while simultaneously enabling atomically precise anchoring of Co sites. This photothermal shock approach operates on a non-equilibrium timescale, presenting a novel pathway for synthesizing atomically precise active sites on highly crystalline supports, a goal that has been difficult to achieve with conventional time-intensive methods. Finally, we confirm the proof-of-concept application of this material as a durable self-supported electrocatalyst for the OER.

The process begins with the fabrication of the conductive CNF scaffold, where as-spun polyacrylonitrile nanofibers (PAN NFs) are first stabilized at 250 °C for 2 hours and subsequently carbonized at 1500 °C for 2 hours (Fig. 1). After an O_2 plasma treatment to render the CNF surface hydrophilic (Fig. S1), a uniform, amorphous vanadium oxide layer was conformally coated onto the CNF *via* a electrodeposition process (Fig. S2a). This method was specifically chosen as it is a simple and robust technique for preparing binder-free electrodes.[24] It ensures intimate VO_x–CNF contact, which is crucial for efficient heat transfer during the shock and for optimal electrochemical application. To optimize sufficient loading while preserving electronic conductivity—avoiding the passivation caused by an excessively thick layer (Fig. S2b and S3)—a deposition time of 10 minutes was selected as the optimal condition (VO_x/CNF). Then, VO_x/CNF was confirmed to have a uniform distribution of V and O on the CNF support (Fig. S4) with initial vanadium oxidation states of both V^{4+} and V^{5+} (Fig. S5).

The profound structural transformation induced by the photothermal shock was investigated by transmission electron microscopy (TEM). The as-prepared VO_x/CNF, with a 20–40 nm thick VO_x layer electrodeposited on CNF, exhibits the characteristic features of an amorphous structure, lacking any long-range atomic order (Fig. 2a). In contrast, after the application of a single photothermal shock, the VO_x layer undergoes a dramatic transformation into a highly crystalline structure without significant change in its thickness (Fig. 2b). High-resolution TEM imaging clearly reveals well-defined lattice fringes with an interplanar spacing of 0.40 nm, which corresponds to the (101) plane of orthorhombic V_2O_5. A single 20 ms pulse instantaneously spikes the temperature to approximately 700 °C and 1600 °C for energy densities of 8 J cm^{-2} and 10 J cm^{-2} (hereafter, denoted as VO_x/CNF-L and VO_x/CNF-H, respectively), providing sufficient activation energy for crystallization followed by rapid cooling (Fig. 2c). Furthermore, the final crystalline phase of the vanadium oxide can be engineered by tuning the applied photothermal energy, as confirmed by the X-ray diffraction (XRD) patterns revealing a clear energy-dependent phase evolution (Fig. 2d). The initial amorphous VO_x/CNF shows only broad halos, indicative of its non-crystalline nature. In contrast, VO_x/CNF-L displays a mixture of crystalline phases, primarily dominated by VO_2 (blue square, JCPDS No. 44-0252), alongside V_2O_5 (gray star, JCPDS No. 41-1426) and V_6O_{13} (yellow circle, JCPDS No. 43-1050). Intriguingly, while VO_x/CNF-H also contains a significant of VO_2 phase, it is further characterized by the emergence of more reduced phases, including V_3O_5 (purple triangle, JCPDS No. 38-1181) and V_2O_3 (green heart, JCPDS No. 34-0187). Moreover, VO_x/CNF-H features slightly lower crystallinity compared to the VO_x/CNF-L, as evidenced by broader XRD peaks (*e.g.*, full

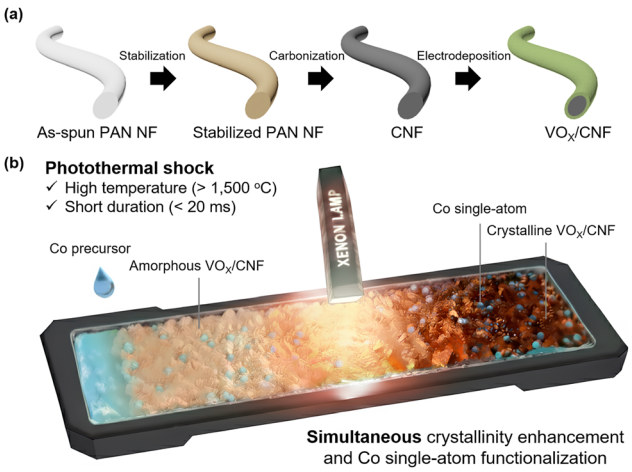

Fig. 1 (a) Schematic illustration of fabrication of amorphous VO_x on CNF. (b) Schematic illustration of the synthesis of Co/VO_x/CNF *via* ultrafast photothermal shock process, highlighting the simultaneous crystallinity enhancement and Co single-atom anchoring.

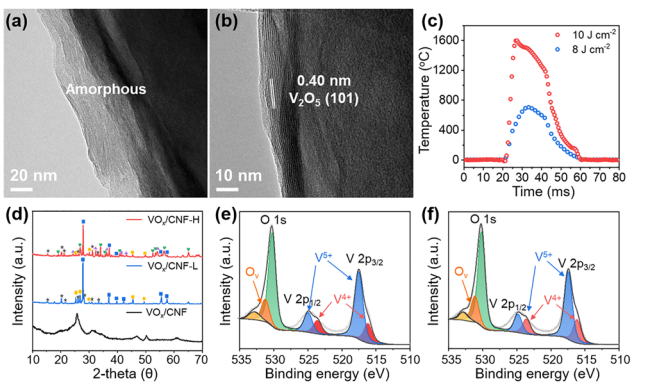

Fig. 2 (a) TEM image of amorphous VO_x/CNF before the shock and (b) crystalline V_2O_5/CNF after the shock. (c) A temperature-time curve of VO_x/CNF during a 20 ms shock at energy densities of 8 J cm^{-2} (VO_x/CNF-L) and 10 J cm^{-2} (VO_x/CNF-H). (d) XRD pattern of VO_x/CNF, VO_x/CNF-L, and VO_x/CNF-H. (e) XPS spectra of VO_x/CNF-L and (f) VO_x/CNF-H in O 1s and V 2p regions.

width at half maximum (FWHM) of main peak near 27° 2θ is 0.14 *vs.* 0.12). These combined characteristics are attributed to the effects of the ultrafast heating and cooling process, which inherently generates a high concentration of intrinsic defects.[25] Specifically, the high-energy photothermal shock in a carbon-mediated reducing microenvironment strips lattice oxygen to create abundant vacancies that locally disrupt long-range ordering, while the subsequent rapid cooling stabilizes this defect-rich state. This energy-dependent phenomenon is corroborated by X-ray photoelectron spectroscopy (XPS) analysis (Fig. 2e and f). The V 2p spectra reveal an increase in the V^{4+}/V^{5+} area ratio for the VO_x/CNF-H (0.35) compared to VO_x/CNF-L (0.28), while the O 1s concurrently confirm a higher relative area of oxygen vacancies (26.8% *vs.* 24.8%). This simultaneous increase in the relative concentrations of the lower oxidation state (V^{4+}) and oxygen vacancies provides evidence for the partial reduction of V^{5+} induced by the higher shock energy, which aligns with the XRD.

Having confirmed energy-tunable crystallization of the VO_x support, we next investigated simultaneous anchoring of Co SACs during the same ultrafast photothermal shock process. The VO_x/CNF precursor, coated with a Co salt solution, was subjected to the optimized photothermal shock (hereafter, denoted as Co/VO_x/CNF-L (700 °C) and Co/VO_x/CNF-H (1600 °C), respectively). Notably, the XPS Co 2p binding energy in Co/VO_x/CNF-H exhibits a distinct negative shift compared to Co/VO_x/CNF-L (Fig. S6). This shift provides direct evidence of a strong electronic metal–support interaction (EMSI) mediated by the abundant oxygen vacancies.[26] The formation of oxygen vacancies leaves excess delocalized electrons in the lattice, which are transferred to the anchored Co atoms, effectively increasing the electron density on the metal sites. The distribution of the anchored Co atoms of Co/VO_x/CNF-H was confirmed using high-angle annular dark-field scanning transmission electron microscopy (HAADF-STEM) with corresponding energy-dispersive X-ray spectroscopy (EDS) mapping (Fig. 3). The EDS maps show Co signals uniformly distributed with atomic dispersion across the VO_x/CNF surface (Fig. 3a and Fig. S7). HAADF-STEM imaging further verified this, revealing individual Co atoms dispersed on the crystalline vanadium oxide lattice, with no nanoparticles or clusters detected (Fig. 3b and c). To definitively clarify the local environment, Co K-edge Extended X-ray Absorption Fine Structure (EXAFS) reveals a unique splitting of the first coordination shell into short Co–O1 and long Co–O2 interactions, alongside a distinct Co–V scattering path (Fig. 3d and Fig. S8 and Table S1). This confirms that Co atoms of Co/VO_x/CNF-H are firmly anchored within lattice vacancies, inducing a Jahn–Teller-like distortion and a reduced coordination number characteristic of a defect-trapped state.[27–29] Importantly, the millisecond-scale thermal cycle is sufficient to generate Co adatoms from the precursor but is insufficient to permit their surface diffusion and aggregation. The subsequent ultrafast cooling rate immobilizes these adatoms at stable anchoring sites, suppressing the thermodynamic drive toward aggregation and stabilizing the Co SACs in its catalytically active, atomically dispersed state. This strategy also proves to be universal, stabilizing not only Co but also Pt, Ru, and Cu SACs on to VO_x/CNF support, in their catalytically active, atomically dispersed states (Fig. S9–S11).

To assess the practical utility as an OER catalyst, we evaluated the electrochemical performance in alkaline medium (1 M KOH). The polarization curves in Fig. 4a illustrate the synergistic effects of the crystalline vanadium oxide support and the Co SACs anchoring. The crystalline phase in VO_x/CNF-L provides slightly enhanced OER activity compared to its amorphous counterpart (amorphous VO_x/CNF), which can be attributed to the improved intrinsic electronic conductivity and structural stability afforded by crystallinity. Notably, anchoring Co SACs on these crystalline supports (Co/VO_x/CNF-H and Co/VO_x/CNF-L) yields a significant boost in OER performance compared to Co-free VO_x/CNF-L, confirming that the atomically dispersed Co moieties act as the primary active sites, while the crystalline nature of the support is crucial for efficient catalysis. Furthermore, Co/VO_x/CNF-H exhibits enhanced OER activity compared to Co/VO_x/CNF-L. The ultrafast cooling from a higher peak temperature (Fig. 2c) limits the time available for attainment of long-range structural order and promotes a higher concentration of oxygen vacancies, which are known to be highly beneficial for OER.[25,30,31] These oxygen vacancies modulate the

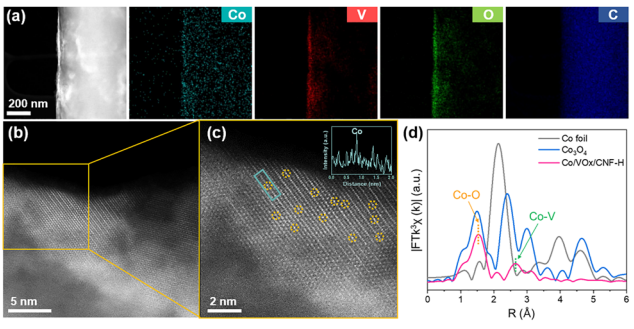

Fig. 3 (a) HAADF-STEM image of Co/VO_x/CNF-H and corresponding elemental distribution maps. (b) High-magnification HAADF-STEM image and (c) magnified image and z-contrast profile of the region highlighted in (b). (d) Fourier transformed k^3-weighted Co K-edge of EXAFS spectra.

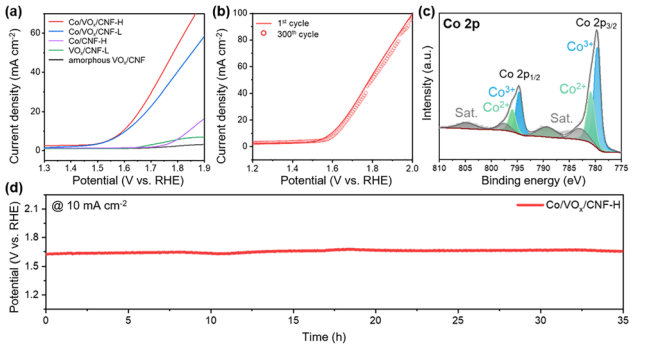

Fig. 4 (a) Polarization curves of Co/VO_x/CNF-H, Co/VO_x/CNF-L, Co/CNF-H, VO_x/CNF-L, and amorphous VO_x/CNF. (b) Polarization curves of Co/VO_x/CNF-H before and after 300 CV cycles. (c) XPS Co 2p spectra of Co/VO_x/CNF-H after 300 CV cycles. (d) Chronopotentiometry curve of Co/VO_x/CNF-H.

local electronic structure of adjacent Co single-atom sites to optimize the adsorption energies of OER intermediates (*e.g.*, *OH, O, OOH) and lower intrinsic kinetic barriers,[32–34] thereby driving the superior OER performance of Co/VO_x/CNF-H alongside the pronounced reduction phases. Consistent with this, a high faradaic efficiency of 95.1% was achieved at 100 mA cm^{-2} (Fig. S12). Moreover, Co/VO_x/CNF-H shows excellent operational durability (Fig. 4b), maintaining a polarization curve nearly identical to its initial state after 300 cyclic voltammetry (CV) cycles (1.3–1.6 V). Regarding the sustained activity, post-OER XPS Co 2p (Fig. 4c) shows an increased Co^{3+}/Co^{2+} ratio, confirming *in situ* reconstruction to active CoOOH species.[35] This surface activation is accompanied by excellent durability, maintaining a stable potential at 10 mA cm^{-2} for over 35 hours (Fig. 4d). This electrochemical robustness is supported by *ex situ* scanning electron microscopy (SEM) analysis (Fig. S13), showing that the self-supported nanofibrous morphology remained intact after the durability test. Furthermore, HAADF-STEM and EDS analysis verify that the Co species remain atomically dispersed without aggregation, demonstrating the exceptional robustness of the active sites (Fig. S14). *Ex situ* XPS analysis of the V 2p region after the OER test (Fig. S15) also reveals a significant decrease in the V^{4+} peak compared to the as-prepared state (Fig. 2f). This suggests that the less stable, lower-oxidation-state V^{4+} species, likely located at the surface, are partially leached or oxidized to V^{5+} during the highly oxidative OER. This phenomenon of vanadium leaching from oxide supports under OER conditions is consistent with prior reports.[14] Despite the partial leaching of the vanadium support, the high activity of Co/VO_x/CNF-H is remarkably preserved. This sustained performance provides compelling evidence that the atomically dispersed Co sites, rather than the vanadium oxide support, are the primary active centers for the OER. In this catalytic system, the highly crystalline vanadium oxide framework primarily serves as a robust scaffold to firmly anchor these Co single-atoms through strong Co–O–V interactions. This durability is clear evidence of the strong atomic anchoring achieved *via* our ultrafast photothermal shock, which robustly anchors the catalytically crucial species against dissolution and aggregation.

In conclusion, we have demonstrated an ultrafast photothermal shock strategy to synthesize Co single atoms anchored on crystalline vanadium oxide. This millisecond process simultaneously achieves the crystallization of the vanadium oxide support and the stable anchoring of Co atoms by kinetically suppressing thermal aggregation. Moreover, the final crystalline phase of the support can be rationally tuned by controlling the energy density. The resulting self-supported electrode successfully served as proof-of-concept application as a durable OER catalyst, presenting a novel and powerful platform for the rational design and scalable fabrication of advanced single-atom catalysts for various energy conversion and storage applications.

D. Jeon: writing, original draft, validation, methodology, and conceptualization. H. Park and J. W. Baek: investigation and editing. K. R. Yoon: editing. S.-J. Kim: editing and supervision. I.-D. Kim: supervision, resources, and funding acquisition.

This work was supported by the Semiconductor-Secondary Battery Interfacing Platform Technology Development Project of NNFC in 2026, the National Research Foundation of Korea (NRF) grant funded by the Korea government (MSIT) (No. RS-2024-00435493 and RS-2023-00236572), and the Korea Institute of Energy Technology Evaluation and Planning (KETEP) and the Ministry of Trade, Industry & Energy (MOTIE) of the Republic of Korea (No. RS-2024-00402410).

Conflicts of interest

There are no conflicts to declare.

Data availability

The data supporting this article have been included as part of the supplementary information (SI). Supplementary information is available. See DOI: https://doi.org/10.1039/d5cc06213f.

References

1 Y. Pan, X. Wang, W. Zhang, L. Tang, Z. Mu, C. Liu, B. Tian, M. Fei, Y. Sun, H. Su, L. Gao, P. Wang, X. Duan, J. Ma and M. Ding, *Nat. Commun.*, 2022, **13**, 3063.
2 H. Jiang, W. Yang, M. Xu, E. Wang, Y. Wei, W. Liu, X. Gu, L. Liu, Q. Chen, P. Zhai, X. Zou, P. M. Ajayan, W. Zhou and Y. Gong, *Nat. Commun.*, 2022, **13**, 6863.
3 L. Gloag, S. V. Somerville, J. J. Gooding and R. D. Tilley, *Nat. Rev. Mater.*, 2024, **9**, 173–189.
4 Y. Zhang, F. Chen, X. Yang, Y. Guo, X. Zhang, H. Dong, W. Wang, F. Lu, Z. Lu, H. Liu, Y. Xiao and Y. Cheng, *Nat. Commun.*, 2025, **16**, 1956.
5 J. Yang, W. Li, D. Wang and Y. Li, *Adv. Mater.*, 2020, **32**, 2003300.
6 F.-Y. Chen, Z.-Y. Wu, Z. Adler and H. Wang, *Joule*, 2021, **5**, 1704–1731.
7 I. S. Filimonenkov, C. Bouillet, G. Kéranguéven, P. A. Simonov, G. A. Tsirlina and E. R. Savinova, *Electrochim. Acta*, 2019, **321**, 134657.
8 J. Bak, H. Kim, S. Lee, M. Kim, E.-J. Kim, J. Roh, J. Shin, C. H. Choi and E. Cho, *ACS Catal.*, 2020, **10**, 12300–12309.
9 L. Tang, Y. Wan and Y. Lin, *Chin. J. Struct. Chem.*, 2024, **43**, 100345.
10 L. Qin, W. Zhang and R. Cao, *Chin. J. Struct. Chem.*, 2023, **42**, 100105.
11 Y. Zhang, B. Wang, C. Hu, M. Humayun, Y. Huang, Y. Cao, M. Negem, Y. Ding and C. Wang, *Chin. J. Struct. Chem.*, 2024, **43**, 100243.
12 P. Hu, P. Hu, T. D. Vu, M. Li, S. Wang, Y. Ke, X. Zeng, L. Mai and Y. Long, *Chem. Rev.*, 2023, **123**, 4353–4415.
13 M. Hussain, M. Nadeem, H. Sun, S. Karim, A. Nisar, M. Khan and M. Ahmad, *Mater. Chem. Phys.*, 2015, **159**, 19–24.
14 S. Prabu, M. Subramani, B. K. Chang and K.-Y. Chiang, *ACS Appl. Nano Mater.*, 2025, **8**, 14083–14094.
15 Y.-H. Choi, *Nanomaterials*, 2022, **12**, 939.
16 C. Youn, S. Shin, K. Shin, C. Kim, C.-L. Park, J. Choi, S. H. Kim, S. Y. Yeo, M. W. Shin, G. Henkelman and K. R. Yoon, *Chem. Catal.*, 2022, **2**, 1191–1210.
17 M. Krbal, V. Prokop, A. A. Kononov, J. R. Pereira, J. Mistrik, A. V. Kolobov, P. J. Fons, Y. Saito, S. Hatayama, Y. Shuang, Y. Sutou, S. A. Rozhkov, Z. R. Stellhorn, S. Hayakawa, I. Pis and F. Bondino, *ACS Appl. Nano Mater.*, 2021, **4**, 8834–8844.
18 Y. Wang, C. Li, X. Han, J. Bai, X. Wang, L. Zheng, C. Hong, Z. Li, J. Bai, K. Leng, Y. Lin and Y. Qu, *Nat. Commun.*, 2024, **15**, 5675.
19 S. Wang, C. Liu, W. Hao, Y. Zhuang, J. Chen, X. Zhu, L. Wang, X. Niu, J. Mao, D. Ma and Q. Zhao, *Chem. Sci.*, 2025, **16**, 6203–6218.
20 C. Rong, K. Flint, C. Doonan and Y. Chen, *Next Mater.*, 2025, **7**, 100457.
21 J.-H. Cha, S.-H. Cho, D.-H. Kim, D. Jeon, S. Park, J.-W. Jung, I.-D. Kim and S.-Y. Choi, *Adv. Mater.*, 2023, **35**, 2305222.
22 D.-H. Kim, J.-H. Cha, S. Chong, S.-H. Cho, H. Shin, J. Ahn, D. Jeon, J. Kim, S.-Y. Choi and I.-D. Kim, *ACS Nano*, 2023, **17**, 23347–23358.

23 D. Jeon, H. Shin, J.-H. Cha, H. Kim, S. Park, J. Ahn, S.-H. Cho, C. Park, D.-H. Kim, E. Shin, H. Baik, J. Kim, S.-Y. Choi and I.-D. Kim, *ACS Nano*, 2025, **19**, 34235–34247.
24 R. Velayutham, R. Manikandan, C. J. Raj, A. M. Kale, C. Kaya, K. Palanisamy and B. C. Kim, *J. Alloys Compd.*, 2021, **863**, 158332.
25 Y. Liu, R. Lin, B. Guo, C. Chen, Q. Wu, X. Zhang, Q. Huang, I. S. Amiinu and T. Liu, *Mater. Rep.: Energy*, 2025, 100377.
26 Y. Chen, C. Zhang, D. Yao, O. M. Gazit and Z. Zhong, *ACS Appl. Mater. Interfaces*, 2025, **17**, 3404–3417.
27 A. Gaur, J. Sharma, G. Kaur, S. Mhin and H. Han, *Adv. Funct. Mater.*, 2025, e16674.
28 M. Ji, X. Yang, S. Chang, W. Chen, J. Wang, D. He, Y. Hu, Q. Deng, Y. Sun, B. Li, J. Xi, T. Yamada, J. Zhang, H. Xiao, C. Zhu, J. Li and Y. Li, *Nano Res.*, 2022, **15**, 1959–1965.
29 D. O. Scanlon, A. Walsh, B. J. Morgan and G. W. Watson, *J. Phys. Chem. C*, 2008, **112**, 9903–9911.
30 M. Yonemura, H. Nishibata, R. Fujimura, N. Ooura, K. Hata, K. Fujiwara, K. Kawano, I. Yamaguchi, T. Terai, Y. Inubushi, I. Inoue, T. Yabuuchi, K. Tono and M. Yabashi, *Sci. Rep.*, 2022, **12**, 2237.
31 A. S. Makarov, G. V. Afonin, R. A. Konchakov, J. C. Qiao, A. N. Vasiliev, N. P. Kobelev and V. A. Khonik, *Intermetallics*, 2023, **163**, 108041.
32 Z. Zhang, C. Feng, D. Wang, S. Zhou, R. Wang, S. Hu, H. Li, M. Zuo, Y. Kong and J. Bao, *Nat. Commun.*, 2022, **13**, 2473.
33 M.-Q. Yang, K.-L. Zhou, C. Wang, M.-C. Zhang, C.-H. Wang, X. Ke, G. Chen, H. Wang and R.-Z. Wang, *J. Mater. Chem. A*, 2022, **10**, 25692–25700.
34 C. Rong, K. Dastafkan, Y. Wang and C. Zhao, *Adv. Mater.*, 2023, **35**, 2211884.
35 Z. Xiao, Y.-C. Huang, C.-L. Dong, C. Xie, Z. Liu, S. Du, W. Chen, D. Yan, L. Tao, Z. Shu, G. Zhang, H. Duan, Y. Wang, Y. Zou, R. Chen and S. Wang, *J. Am. Chem. Soc.*, 2020, **142**, 12087–12095.

